MRI to PET Cross-Modality Translation using Globally & Locally Aware GAN (GLA-GAN) for Multi-Modal Diagnosis of Alzheimer's Disease

Apoorva Sikka*, Skand*, and Jitender Singh Virk, Deepti R. Bathula

arXiv:2108.02160v1 [eess.IV] 4 Aug 2021

***Abstract*— Medical imaging datasets are inherently high dimensional with large variability and low sample sizes that limit the effectiveness of deep learning algorithms. Recently, generative adversarial networks (GANs) with the ability to synthesize realist images have shown great potential as an alternative to standard data augmentation techniques. Our work focuses on cross-modality synthesis of fluorodeoxyglucose (FDG) Positron Emission Tomography (PET) scans from structural Magnetic Resonance (MR) images using generative models to facilitate multi-modal diagnosis of Alzheimer's disease (AD). Specifically, we propose a novel end-to-end, globally and locally aware image-to-image translation GAN (GLA-GAN) with a multi-path architecture that enforces both global structural integrity and fidelity to local details. We further supplement the standard adversarial loss with voxel-level intensity, multi-scale structural similarity (MS-SSIM) and region-of-interest (ROI) based loss components that reduce reconstruction error, enforce structural consistency at different scales and perceive variation in regional sensitivity to AD respectively. Experimental results demonstrate that our GLA-GAN not only generates synthesized FDG-PET scans with enhanced image quality but also superior clinical utility in improving AD diagnosis compared to state-of-the-art models. Finally, we attempt to interpret some of the internal units of the GAN that are closely related to this specific cross-modality generation task.**

***Index Terms*— Alzheimer's Classification, Cross-Modality Estimation, Generative Adversarial Networks, Medical Imaging**

I. Introduction

Alzheimer's disease (AD) is a chronic neuro-degenerative disorder that interferes with memory, thinking and behavior. It is a progressive disease where symptoms gradually worsen with time, making early diagnosis very crucial. In addition to clinical and behavioral observations, diagnosis of AD is based on neuroimaging assessments. Recently, efforts have been directed towards multi-modal image analysis to identify reliable biomarkers that can aid in accurate diagnosis of AD [1]. As multiple imaging modalities capture complementary information related to different aspects of the disease, their synergistic fusion increases the efficacy of diagnosis. While gray matter atrophy and ventricular enlargement observed in magnetic resonance imaging (MRI) are established markers for pathology, patterns of neuronal uptake and cerebral distribution of fluorodeoxyglucose (FDG) in positron emission tomography (PET) is also an essential discriminating factor for AD [2]. Consequently, the joint analysis of MRI and PET is now a standard evaluation for AD [3]–[5]. However, acquiring different modality scans for all patients is not always feasible due to high cost, increased risk of radiation exposure and limited access to imaging facilities. While MRI scanners are quite pervasive, PET technology is not yet common. Our work focuses on cross-modality estimation of FDG-PET scans from MR images using generative models. We further assess the quality of the synthesized PET images based on their potential to diagnose AD.

With recent advances in machine learning, several studies have focused on the task of image-to-image translation that involves transforming images from one domain to another. [6] used a structured random forest-based model along with an auto-context model to translate MRI patches into computed tomography (CT) for attenuation correction in PET. Similarly, a regression forest-based framework was developed in [7] for predicting a standard-dose brain FDG-PET image from a low-dose PET image and its corresponding MRI. Regression forests have also been used by [8] to reconstruct a FLAIR image given the corresponding T1-weighted, T2-weighted, and PD-weighted images of the same subject.

In the past few years, Generative Adversarial Networks (GAN) [9] have achieved remarkable success due to their versatility in synthetic image generation with potential applications across various domains [10], [11]. GANs are being utilized extensively in the field of medical image analysis to perform a wide range of tasks including denoising, reconstruction, segmentation, classification etc. [12], [13], [14], [15], [16]. The ability of GANs to generate diverse and realistic image samples makes them especially appealing to the medical domain that suffers from a lack of large, annotated datasets. Before GANs, other generative

* denotes equal contribution (Corresponding authors: Deepti R. Bathula.)

Apoorva Sikka, Jitender Singh Virk and Deepti R. Bathula are with the Department of Computer Science & Engineering, Indian Institute of Technology Ropar, Punjab - 140001, India (e-mail: apoorva.sikka@iitrpr.ac.in, jitendersinghvirk47@gmail.com, bathula@iitrpr.ac.in).

Skand, is with Oregon State university, Corvallis, OR 97331, United States (e-mail: pvskand@protonmail.com).

models like Autoencoders [17] and Variational Autoencoders (VAE) [18] were also utilized. Several variants of GANs have been proposed to tackle cross-modality estimation or data augmentation in the medical domain. Conditional GANs, where image generation is conditioned on external information, have been used in many cross-modality image translation tasks such as MRI to CT [19], CT to MRI [20], etc. To reduce radiation dose, [19] employed context-aware GANs to predict CT scans from MR scans using an image gradient difference loss function. Although MR and CT represent different imaging modalities, they both capture details of anatomical structures.

A more challenging cross-modality synthesis task involves predicting functional scans from their corresponding structural scans. In [21], PET images are estimated from CT scans using a mixed Fully Convolutional Network (FCN) and a conditional GAN approach where the output of FCN is fed in addition to the CT scan as an input using only pixel-wise and adversarial loss. A sketcher-refiner based adversarial training has also been employed to predict PET-derived demyelination from multi-modal MRI including measures derived from diffusion tensor imaging (DTI) [22]. [23] used a patch-based convolutional neural network (CNN) to capture non-linear mapping between PET and MRI. [1] attempted to find a relationship between brain atrophy (MRI) and hypometabolism (PET) using a computationally tractable formulation of partial least squares regression (PLSR). Their main aim was to explore non-local intensity correlations between these modalities through PLSR. [24] proposed a global 3D U-Net based formulation to predict the PET from MR. Recently, [25] proposed an image-to-image translation framework based on 3D cycle-consistent GAN (3D-cGAN) for synthesizing PET images from MRI. Cycle GANs were originally introduced to train unsupervised image translation models using the GAN architecture. DUAL-GLOW, by [26], is another MRI to PET modality transfer technique based on the flow-based generative model [27]. This formulation is based on two flow-based invertible networks and a relation network that maps the latent spaces to each other.

As observed from previous studies [23], a purely local approach is not capable of capturing true relationship between two complex modalities. This knowledge necessitates the use of global approaches that can capture non-local, non-linear correlations. However, previous attempts [24] also indicate that an entirely global approach fails to represent finer structures and details effectively. We hypothesize that the quality of the synthesized PET scans can be improved by exploiting both global and local contexts simultaneously within a GAN architecture. Furthermore, majority of the previous studies used per-pixel loss functions that tend to generate blurry target images with loss of details as well as cause artifacts [28]. Consequently, we propose to use alternative loss functions that tackle these issues. As SSIM is widely used to evaluate the quality of reconstructed images, we use a multi-scale version of SSIM (MS-SSIM) as an additional objective function to assess image quality and ensure structural consistency at different scales [29]. In addition, as Alzheimer's related literature suggests significant variation in regional sensitivity to the disease progression, we propose to enforce local contextual integrity using region-wise loss based on anatomical delineation. The main contributions of our work are the following:

- We propose a novel end-to-end, globally and locally aware image-to-image translation GAN (GLA-GAN) with a multi-path architecture that ensures both global structural integrity and fidelity to local details.
- We supplement the standard adversarial and voxel-level loss terms with objective functions that ensure structural consistency over multiple resolutions as well as local contextual integrity based on anatomical brain regions
- We provide extensive evaluation of our proposed GLA-GAN against state-of-the-art techniques using numerous quality assessment metrics. Additionally, we demonstrate the potential of synthesized PET scans to improve multi-modal Alzheimer's disease classification accuracy.
- Finally, we attempt to gain better understanding by identifying, visualizing and interpreting internal GAN features. We present some units that are closely related to both common and differential FDG uptake patterns in PET images.

II. Methods

GANs have been used extensively for generating images for a variety of tasks in computer vision. GANs have two competing neural networks, a generator (G) and a discriminator (D), that are trained simultaneously in a min-max fashion. The goal of the generator is to create realistic-looking synthetic images to fool the discriminator, while the discriminator tries to distinguish between the real and synthetic samples. This competition helps GANs to analyze, capture and mimic the variations within the dataset effectively. Here we use a variant of GAN where source modality image as an input controls and guides the generator to estimate the target modality image.

Let $\{X_{i=1}^{N}\}$ represent MRI scans and $\{Y_{i=1}^{N}\}$ represent PET scans of N subjects in the training set with dimensions $x_1 \times x_2 \times x_3$ and $y_1 \times y_2 \times y_3$ respectively. Hence, $\{X_i, Y_i\}$ represents the i^{th} subject-specific source-target paired data. The goal is to learn a data-driven mapping function $f : X \longrightarrow Y$ that accurately predicts the target PET image (Y) for any new input MR image (X). Unlike natural image translation, the mapping between multi-modal medical images can be very complex and highly non-linear. More specifically, as MRI and PET represent structural and functional images of the brain, respectively, they lack local spatial consistency between modalities. This knowledge necessitates the use of global approaches that can capture non-local correlations. However, a purely global approach might not be capable of representing

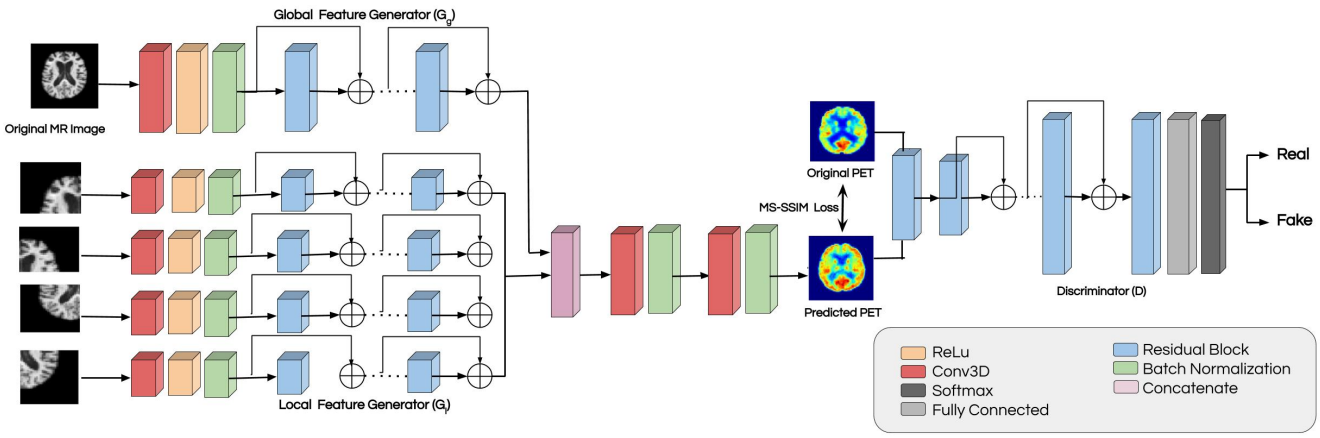


Fig. 1: Proposed globally and locally aware image-to-image translation GAN (GLA-GAN) architecture for cross-modal PET estimation from MRI using L_1, MS-SSIM and ROI based objective function. [Best viewed in color]

finer structures and details effectively. Our proposed solution combines locally extracted features with global attributes to enhance PET synthesis.

A. Globally & Locally Aware GAN (GLA-GAN)

To this extent, we developed a GAN based framework with multi-path architecture that discerns both global structures and local texture. Figure 1 provides an overview of the proposed multi-path GAN framework for MRI to PET cross-modality transfer. Here we provide details of the architecture including a description of the generator and discriminator along with the loss formulation of our method.

1) Generator: The generator G of our GLA-GAN is a combination of multiple sub-networks. It consists of two modules namely, a *global module* (G_g) and a *local module* (G_l). The global module is a generator network that maps the complete MR image of dimensions $64 \times 64 \times 64$ to a latent feature space f_g via a set of residual blocks [30]. For an input image X, the output of global network is $G_g(X) \in R^{64 \times 64 \times 64 \times f_g}$. The local module is a set of K generator networks which work independently on K disjoint patches that cover the whole MR image. Each local network maps an input patch (X_k) to a feature vector f_l^k and outputs $G_l(X_k) \in R^{32 \times 32 \times 64 \times f_l^k}$. The k obtained patches are fused together to form $64 \times 64 \times 64$ before passing to next layer. The underlying architecture of G_g and each of G_l^k is a set of four residual blocks with batch normalization [31] and rectified linear unit (ReLU) activation [32]. The two sets of features (f_g and f_l^k where $k = 1$ to K) are directly concatenated channel-wise which maintains their spatial order and passed through two convolutional layers followed by sigmoid activation to regress the intensity values of the target PET image.

.

ResNet Block - In general, the architecture of most generator modules is a 10-layer ResNet proposed by [30]. The basic idea behind ResNet is the introduction of skip connections between layers of a convolution neural network to preserve the input from previous layers. This approach mitigates the gradient degradation problem that is caused by increase in number of layers in a network and avoids any loss in the information. Our proposed generator network has four residual blocks alongside four convolution layers. The number of convolutional filters is 64, 64, 128, and 64 respectively with kernel size of 3×3 and stride 1. On the lines of [33], we also use batch normalization [34] after every convolutional layer along with LeakyReLu as the activation function.

2) Discriminator: The discriminator module, D, is a simple classification network that forces the generator to produce realistic and coherent PET images. This is achieved by coercing the generator to learn the underlying data distribution by inferring if the generated PET images are real or fake. The discriminator network is a CNN with six convolution layers followed by batch normalization and leaky ReLU activation function for the first five layers and a sigmoid activation after the last layer. The kernel size is $4 \times 4 \times 4$ for first four layers and $2 \times 2 \times 2$ for next two layers, and the numbers of the filters in each layer are 64, 128, 256, 512, 64 and 1 respectively.

B. Synthesis Loss function

The objective function used in our GLA-GAN framework is a combination of multiple loss terms that coerce the network towards to the most feasible distribution representing real dataset.

1) Adversarial Loss: The loss function for the generator is implicit as it learns based on discriminators performance during training. On the other hand, the discriminator is updated by minimizing the adversarial loss function as given below:

$$\mathcal{L}_G(D,G) = \mathbb{E}_{y\sim Y}(y)[\log D(y)] + \mathbb{E}_{x\sim X}[\log(1 - D(G(x)))] \quad (1)$$

The idea is to minimize this objective function so that D be as confused as possible to distinguish between real and generated PET images to help G generate increasingly realistic PET scans. However, due to the intricate nature of medical images, only adversarial loss cannot be sufficient to generate high quality scans that have same uptake as real PET scans. To mitigate this, we propose to incorporate additional terms in the loss function that penalize loss of detail to enhance the quality of synthesized scans as described below.

2) Voxel-wise L_1 Reconstruction Loss: Least absolute deviations (L_1) or voxel-wise reconstruction loss is a standard loss function defined as:

$$\mathcal{L}_{L_1} = \frac{1}{n}\sum_{i=1}^{n} |y_i - \hat{y}_i| \quad (2)$$

where y_i and $\hat{y}_i$ are the intensity values of the voxels in the estimated and real PET scans. By minimizing the sum of all the absolute differences across voxels, L_1 loss trains the network to understand the differences between images at a voxel level.

3) Multi-Scale SSIM Loss: In addition to adversarial loss, we wanted to enforce the structural similarity in images that encourages structure of the generated PET to be similar to that of the ground truth PET. Structural similarity index (SSIM) is one such metric that is used to evaluate the quality of images in image processing algorithms. Single scale SSIM is computed as follows:

$$\text{SSIM}(x,y) = [l(x,y)]^{\alpha}.[c(x,y)]^{\beta}[s(x,y)]^{\gamma} \quad (3)$$

where $l(x,y)$, $c(x,y)$ and $s(x,y)$ are luminance, contrast and structure measures of the image, and α, β and γ are weight parameters that assign importance of each of the measures. When $\alpha = \beta = \gamma = 1$, the above formulation can be reduced to:

$$\text{SSIM}(x,y) = \frac{(2\mu_x\mu_y + C_1)(2\sigma_{xy} + C_2)}{(\mu_x^2 + \mu_y^2 + C_1)(\sigma_x^2 + \sigma_y^2 + C_2)} \quad (4)$$

where x is the estimated PET and y is the ground truth PET. μ_i is the mean of image i, σ_i is the variance of image i and σ_{xy} is the co-variance of images x and y. C_1 and C_2 are empirically found constants in order to best perceive the structure of the estimated image with respect to the ground truth image.

Given that SSIM is differentiable, it can be easily used as a cost function to induce sensitivity to changes in the structure. However, SSIM is only sensitive to the scale at which local structure is analyzed. Hence, [35] proposed a multi-scale variant known as multi-scale structural similarity index (MS-SSIM) that computes SSIM at multiple scales. In order to compute MS-SSIM for S scales, the image are downsampled by a factor by 2 for $S-1$ times and are combined using the following formulation:

$$\text{MS-SSIM}(x,y) = w(s) \times [l(x,y)].\prod_{j=1}^{S}[c_j(x,y)]^{\beta_j}[s_j(x,y)]^{\gamma_j} \quad (5)$$

$$L_{\text{MS-SSIM}} = 1 - \text{MS-SSIM} \quad (6)$$

where $l(x,y)$, $c_j(x,y)$ and $s_j(x,y)$ are the luminance, contrast and structure components of the image and $w(s)$ is the weight factor for the scale S. In all our experiments, we use empirically determined parameter values: three levels of resolution ($S = 3$) and weights as $w(1) = 0.0448$, $w(2) = 0.2856$ and $w(3) = 0.3001$. This approach ensures structural consistency across multiple resolutions and thus improves the visual quotient of the generated PET scans.

4) Region of Interest (ROI) Loss: While the L_1 loss ensures voxel level fidelity of intensity values, the perceptual similarity metric facilities global structural similarity at multiple scales. However, both of these terms represent summary statistics that consider the image as a whole. As past studies suggest that there is significant variation in regional sensitivity to Alzheimer's across subjects [36], we propose to enforce local contextual integrity using region-wise loss based on anatomical delineation. We hypothesize that supplementing L_1 and MS-SSIM loss with region-based loss can help capture discriminating features between the two classes and thus help GAN to reliably learn a bimodal distribution. Consequently, we used the Automated Anatomical Labeling (AAL) atlas to segment each MRI scan into 116 ROIs and calculated mean intensity of all 116 ROIs for both real and generated PET data. These average intensities were used as feature vectors to compute mean-squared ROI loss as follows:

$$\mathcal{L}_{ROI} = \frac{1}{R}\sum_{i=1}^{R}[\frac{1}{N_R}\sum_{j=1}^{N_R}(y_{ij} - \hat{y}_{ij})]^2 \quad (7)$$

where R is number of ROIs, N_R is number of voxels in ROI R, y_{ij} and $\hat{y}_{ij}$ are the true and predicted voxel intensity values from ground truth and synthesized PET scans respectively.

5) Combined Objective Function: All the modules or sub-networks in the framework are jointly optimized using the following objective function, specially curated for MRI to PET cross-modality estimation:

$$\mathcal{L} = \lambda_G\mathcal{L}_G + \lambda_{MS-SSIM}\mathcal{L}_{MS-SSIM} + \lambda_{L1}\mathcal{L}_{L1} + \lambda_{ROI}\mathcal{L}_{ROI} \quad (8)$$

where λ_G, $\lambda_{MS-SSIM}$, λ_{L1} and λ_{ROI} are weighing factors for GAN, perceptual, voxel-wise and ROI based loss terms respectively.

III. Experiments

A. Dataset

We conducted all our experiments on Alzheimer's Disease Neuroimaging Initiative (ADNI) database (adni.loni.usc.edu). The ADNI is a longitudinal study designed to develop clinical, imaging, genetic, and biochemical biomarkers for the early detection and tracking of Alzheimer's disease (AD) [37]. Subjects in the dataset are categorized as either cognitively Normal (CN) or Alzheimer's disease (AD). We collected a total of 402 samples from ADNI-1 & ADNI-2 having both prepossessed MRI and FDG-PET modalities (CN-241, AD-161). Further, we collected 179 samples from ADNI-1 & ADNI-2 which had only MRI scans (CN-83, AD-79). We refer to the first subset with both modalities as **Paired** and fusion of these two subsets as **Incomplete** datasets respectively. Lastly, multiple sets of **Complete** dataset are created by adding synthesized versions of missing PET scans to the Incomplete dataset using various models.

Details of the image acquisition protocols along with initial preprocessing for ADNI-1 and ADNI-2 scans are described in [38], [39] respectively. A standard sequence of pre-processing steps have been employed to prepare the data for analysis. Firstly, MR images were Anterior Commisure (AC)-Posterior Commisure (PC) corrected using SPM12 [40]. Then skull stripping of MR images was performed using ROBEX [41] followed by intensity normalization and linear alignment to MNI template using FSL package [42]. Subsequently, PET image were aligned to MRI using the same linear registration. This brings both MRI and PET images to Montreal Neurological Institute (MNI) space with size $90 \times 109 \times 90$ which were further resized to $64 \times 64 \times 64$. Sub-sampling was performed to accommodate network size to fit into the memory. Finally, MRI images were segmented into gray matter (GM), white matter (WM) and cerebro-spinal fluid (CSF) using FSL. The GM and WM are further segmented into ROIs according to AAL atlas and the mean intensity of each ROI was used as a feature for AD classification.

B. Experimental Setup

All the experiments were conducted using Pytorch [43]. We trained the network in an end-to-end fashion with a batch size of 4, using Adam optimizer [44] with a momentum of 0.1 and learning rate of 0.00002.

1) Comparison with state-of-the-art methods: We investigated the efficacy of our proposed methodologies by comparing them to different approaches developed specifically to address MRI to PET modality transfer. Although most of the related studies used the ADNI dataset, the sample subset chosen to conduct experiments varied across them. To ensure fair comparison, we accurately re-implemented three of the state-of-the-art networks: 3D U-Net based autoencoder [24], Conditional GAN [45] and Cycle-GAN [25]. A comprehensive evaluation of all the methods is performed using both qualitative and quantitative assessment tools. We used the standard k-fold cross-validation with 5 folds to evaluate the models. In addition to the quality of the synthesized PET images, the models are also evaluated based on the utility of the predicted PET scans in a downstream Alzheimer's disease classification task. Following is a brief description of the metrics used to evaluate the quality of the synthesized images.

Mean Absolute Error is a commonly used metric for prediction problems to measure the magnitude of voxel-wise intensity differences. It is an arithmetic average of the absolute differences the estimated and true intensity values. It is computed as follows:

$$MAE = \frac{1}{n}\sum_{i=1}^{n}|y_i - \hat{y}_i| \tag{9}$$

where y_i and $\hat{y}_i$ are the intensity values of the voxels in the predicted and ground truth PET scans respectively.

Peak Signal-to-Noise Ratio (PSNR) is most commonly used to measure the quality of reconstruction algorithms. The metric is a ratio of maximum power of a signal and the power of distorting noise that affects the fidelity of its representation. It is generally expressed in terms of the logarithmic decibel scale. It is computed as follows:

$$PSNR = 10\ log_{10}\left(\frac{MAX^2}{MSE}\right) \tag{10}$$

where MAX is the maximum possible intensity of the image and MSE is the mean squared error between the estimated and ground truth PET image. Higher value of PSNR is indicative of better synthesis quality.

Structure Similarity Index (SSIM) compares the similarity in structures of the two images instead of comparing individual voxel values as explained in section II-B.3

2) Alzheimer's Classification: In addition to the quality of the synthesized PET scans, we showcase the potential of the generated PET scan to facilitate in binary Alzheimer's disease classification (AD vs Normal). Towards this end, we used GM and WM segmentation first and did the Automated Anatomical Labeling (AAL) atlas to segment each MR image into 116 ROIs and calculated mean intensity of all ROIs. These average intensities taken from both the modalities lead to a feature vector of size $116 * 4$. This final feature vector was used to train a support vector machine (SVM) using a radial basis function (RBF) kernel for multi-modality AD classification. We use several standard classification performance metrics such as accuracy (ACC), sensitivity (SENS), specificity (SPEC), Area under the curve (AUC), Matthews correlation coefficient (MCC) and F1-score to evaluate the models.

IV. Results & Discussion

We demonstrate the merits of our proposed model based on quality of synthesized PET scans as well as their potential

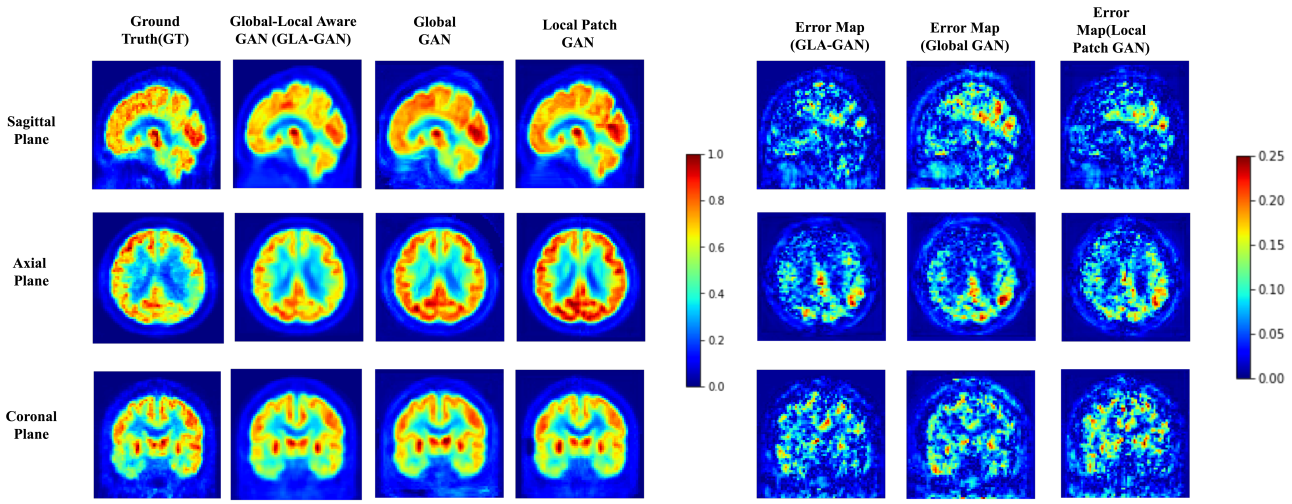


Fig. 2: (a)

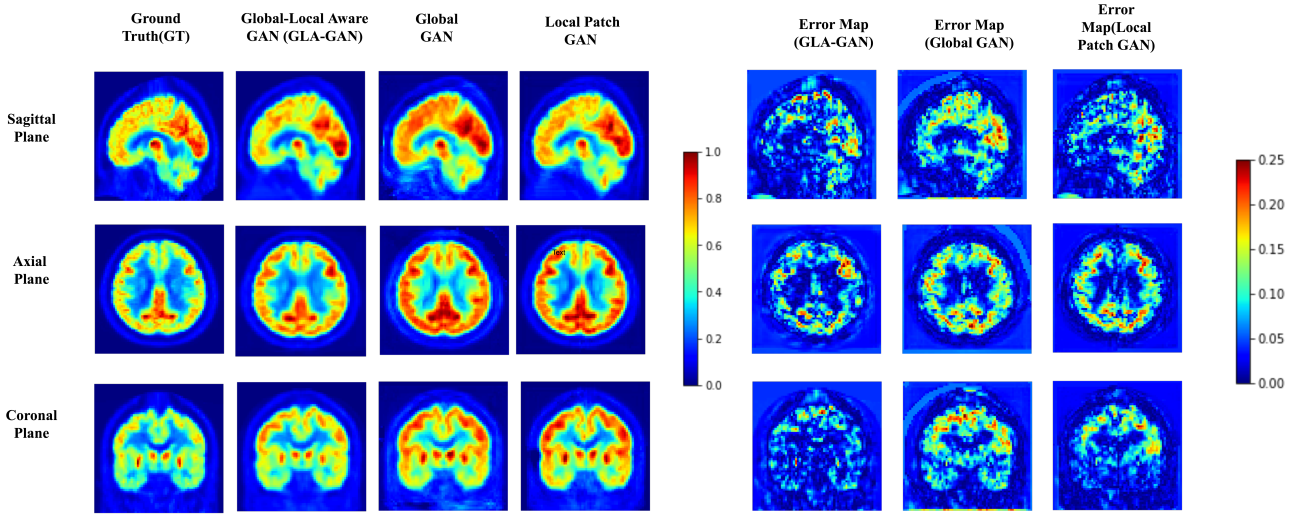


Fig. 3: (b)

Fig. 4: Qualitative comparison of PET scans synthesized using GLA-GAN, Global-GAN and patch based Local-GAN. Ground truth and estimated PET scan along with error maps corresponding to each of the models is presented for an AD (a) and CN (b) sample in axial, coronal and sagittal views. [Best viewed in color]

for accurately diagnosing AD. Additionally, we evaluate the effectiveness of different modules of the mutli-path GAN architecture and illustrate the benefits of various loss components through ablation studies. We have compared our method only with other deep learning variants as they were proved to be better than traditional ML methods. Finally, we visualize and interpret some internal GAN units in the context of this particular generation task.

A. PET Synthesis

Firstly, we demonstrate the significance of incorporating both global and local contextual information simultaneously through parallel modules in the GLA-GAN framework. To this end, we compare three variants of the multi-path architecture: (i) Global GAN, (ii) Local GAN and (iii) Global-Local GAN. Figures 4 (a) and (b) show qualitative visualizations of PET scans synthesized using these three models along three planes (axial, sagittal and coronal) for an AD and CN sample respectively. In addition to the generated images, error maps with respect to the ground truth are also presented. Although not readily apparent, there are subtle differences in the estimates generated by the individual Global and Local

Method	SSIM	PSNR	MAE
U-Net	96.496± 0.00056	28.928 ± 0.26	0.015±0.2383
GAN-L1-SSIM	**96.974 ± 0.181**	**29.50± 0.019**	0.0144±0.0007
Cycle GAN	96.148±0.004	23.194±0.22	0.0142±0.005
GLA-GAN	96.88 ± 0.26	29.326± 0.06	**0.01372 ±0.001**

TABLE I: Comparison of PET synthesis quality using different metrics. SSIM - Structural Similarity Index, PSNR - Peak Signal-to-Noise Ratio, MAE - Mean Absolute Error. Results are shown as mean ± standard deviation.

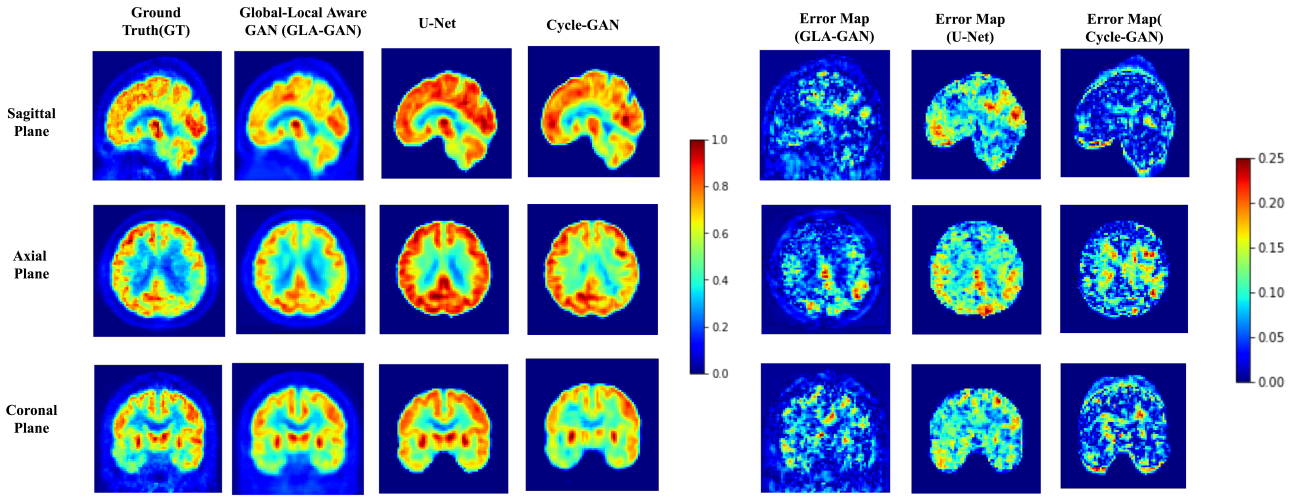


Fig. 5: (a)

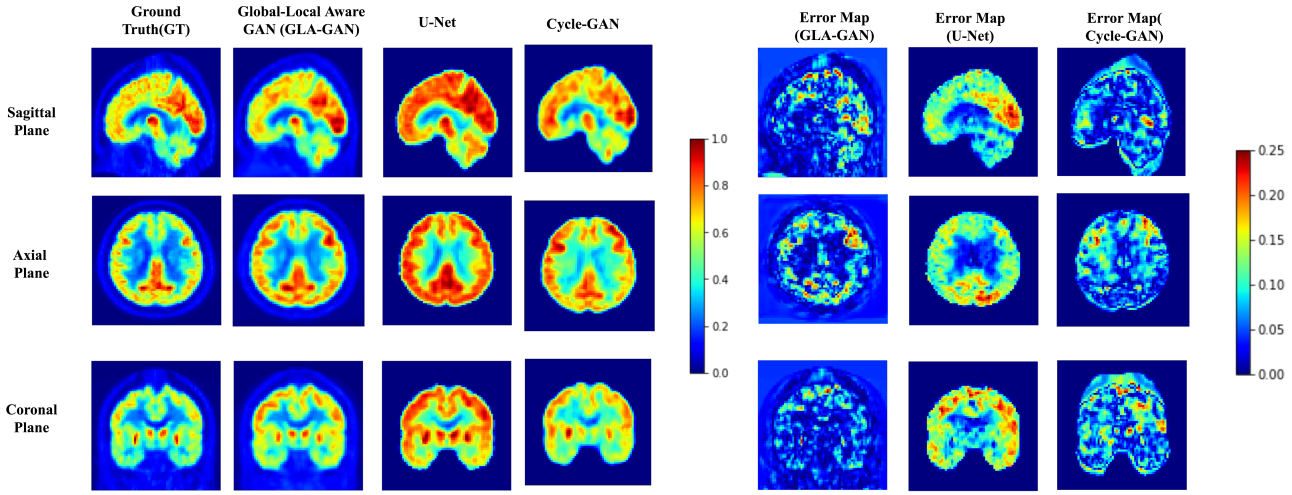


Fig. 6: (b)

Fig. 7: Qualitative comparison of PET scans synthesized using GLA-GAN, 3D-U-NET and Cycle-GAN. Ground truth and estimated PET scan along with error maps corresponding to each of the models is presented for an AD (a) and CN (b) sample in axial, coronal and sagittal views. [Best viewed in color]

only modules. A closer observation reveals that while the local module is better at capturing intricate details like the shape of ventricles, the global module achieves better estimate of the FDG uptake intensity. However, it is clearly evident from both synthesized images and error maps that the hybrid model predicts the FDG uptake patterns for both classes of samples (AD and CN) most accurately.

Next, we benchmarked our proposed GLA-GAN model against three state-of-the-art models: (i) 3D U-NET based autoencoder [24], (ii) Standard GAN with L1 & SSIM Loss terms and (iii) Cycle-GAN [25]. Figure 7 shows qualitative comparison of GLA-GAN with these three models. As Cycle-GAN is based on a global transformation framework, it is able to discern general variations in uptake patterns of AD and CN classes. However, it fails to capture local contextual details as evident from the discrepancy in the shape and uptake in ventricles depicted in both the axial and coronal planes when compared to the ground truth PET scan. On the other hand, the 3D U-NET produced very generic and blurry estimates of the real PET scans. In comparison to these global methods, the results clearly indicate the superiority of our GLA-GAN model in accurately synthesizing PET scans without loss of details. Additionally, quantitative evaluation of these models based on three quality assessment metrics is provided in Table I. The GLA-GAN framework provides either on-par (statistically insignificant difference) or better performance than competing methods across these metrics. While it provides the lowest MAE, there was no significant difference for PSNR and SSIM ($p = 0.1690$ and $p = 0.1363$ using paired, two-tailed, T-test) when compared to the best performing model.

B. AD Classification

In addition to the quality of images, potential clinical utility of the generated scans is of great significance in the medical domain. Hence, we evaluate the models on their capability to synthesize PET scans that improve AD diagnostic accuracy.

Method	Accuracy	Sensitivity	Specificity	F1-Score	MCC	AUC
U-Net	0.8325±0.02	0.7895±0.021	0.8664±0.016	0.7910±0.023	0.6559±0.015	0.9191±0.005
Simple-GAN (L1 + MS-SSIM)	0.8406±0.005	0.7983±0.007	0.8717±0.009	0.8004±0.005	0.6735±0.01	0.9247±0.005
Cycle GAN	0.8326±0.02	0.8192±0.02	0.8795±0.08	**0.8369±0.03**	0.6917 ± 0.027	0.9209±0.008
GLA-GAN(L1+MS-SSIM+ROI)	**0.8456 ± 0.007**	**0.8330 ± 0.006**	**0.8900±0.005**	0.8256± 0.007	**0.7198 ± 0.013**	**0.9314±0.004**

TABLE II: AD Classification Results: Comparison of models across standard classification performance metrics for the Paired dataset. Results are shown as mean ± standard deviation.

Method	Accuracy	Sensitivity	Specificity	F1-Score	MCC	AUC
Only MRI	0.8293±0.016	0.803±0.035	0.8537± 0.041	0.8047±0.022	0.6557± 0.034	0.9035± 0.019
U-Net	0.8289±0.007	0.7947±0.012	0.8597±0.003	0.8029±0.009	0.6559±0.015	0.9128±0.005
Simple-GAN (L1 + MS-SSIM)	0.8223±0.003	0.7819±0.005	0.8573±0.003	0.7940±0.003	0.6406±0.006	0.9072±0.001
Cycle GAN	0.8352±0.020	0.8133±0.018	0.8796±0.04	**0.8379±0.021**	0.6949 ± 0.024	0.916±0.060
GLA-GAN(L1+MS-SSIM+ROI)	**0.845 ± 0.004**	**0.8343 ± 0.005**	**0.8919 ± 0.004**	0.8292± 0.01	**0.7235 ± 0.001**	**0.9299±0.003**

TABLE III: AD Classification Results: Comparison of models across standard classification performance metrics for the Complete datasets (Incomplete dataset augmented with synthesized versions of missing PET scans from each of the models). Results are shown as mean ± standard deviation.

We performed two sets of classification experiments: (a) A 5-fold cross-validation experiment using the Paired dataset where 4 folds were used to train both the generation and classification networks followed by testing on the remaining fold. (b) The generation models were used as data augmentation tools by training them on Paired dataset. The trained models were used to complete the Incomplete dataset by synthesizing the missing PET scans. AD classification was then conducted on the completed dataset. Classification results across all metrics for these two experiments shown in Tables II and III respectively. As the results clearly indicate, the proposed GLA-GAN provides better AD classification accuracy compared to the competing methods.

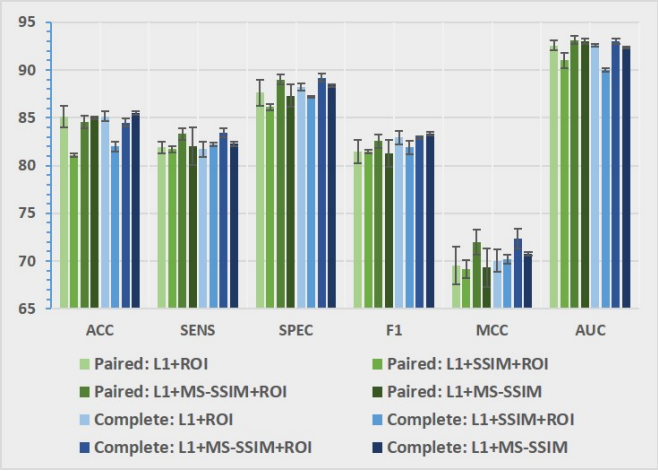


Fig. 8: Evaluation of the GLA-GAN model with different combinations of loss components across standard classification performance metrics on both paired dataset and complete dataset.

C. Ablation Studies

To understand the importance of different loss components and their contribution to the synthesis task, we compare four variations of GLA-GAN models with different combinations of penalty terms: $\mathcal{L}_{L1}$, $\mathcal{L}_{\text{SSIM}}$, $\mathcal{L}_{\text{MS-SSIM}}$, and $\mathcal{L}_{ROI}$. These variants of GLA-GAN were applied to both the paired and complete datasets. The results depicted in Figure 8 establish that ROI based loss contributes the most for improving AD classification. Although classification accuracy is relatively low for ROI combined with SSIM loss, there were no significant differences in other metrics. It can also be noticed that replacement of SSIM with MS-SSIM loss also improves the results indicating the necessity to ensure structural integrity at multiple scales. These results suggest that the constraints imposed by the $\mathcal{L}_{MS-SSIM}$ and $\mathcal{L}_{ROI}$ assist the hybrid model to not only capture the overall structure but also preserve the local regional details. These enhancements to the quality of generation in turn lead to improved multi-modal classification of AD using synthesized PET scans.

We have already established the importance of having both global and local contextual modules to generate superior quality synthesized PET scans. Subsequently, we further explored the impact of number of non-overlapping patches used by the local module on the performance of the model. The results of the experiment conducted with $K = 2, 4$, and 8 are presented in Figure 9. Contrary to our expectations, the performance did not increase with increasing K but with $K = 4$ providing the best results. However, further investigation is needed to explore if anatomically informed rather than generic cuboid patches would be more efficient.

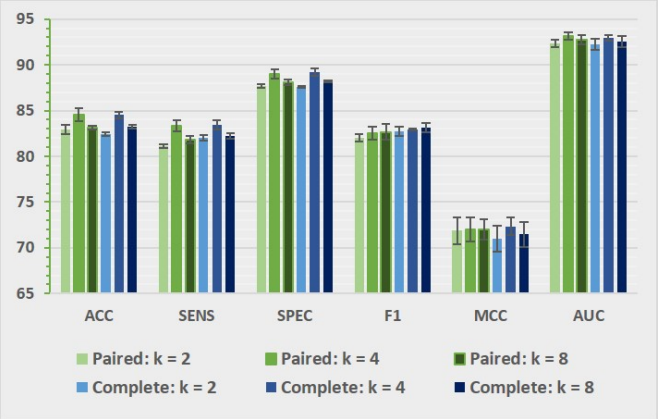


Fig. 9: Evaluation of the GLA-GAN model with varying number of patches (K) used in the local module across standard classification performance metrics on both paired dataset and complete dataset.

D. Understanding GLA-GAN

Recently, explainability of deep learning models has attracted increasing attention. Here, we attempt to gain some insights about their inner workings using interpretation strategies such as exploratory analysis and visualization.

1) Visualization: Visualization of saliency maps has become a standard tool for interpreting the attention of neural networks that is based on backpropagation of gradients. These probabilistic maps are only effective when specific objects or targets of interest exist. For example faces in computer vision applications or lesions in the medical domain. However, for a disorder like AD that is characterized by gross brain atrophy involving many regions and varying significantly across subjects and through disease progression, saliency maps are not very informative.

Although many of the features did not lend themselves readily to human interpretability, we were able identify some features from the global module (G_g) of the GLA-GAN that were relevant to this particular task. Some of the commonly used biomarkers for Alzheimer's include cortical and subcortical atrophy and dilation of ventricles. One of the features characterized these specific brain regions as shown in Figure 10 (a). Furthermore, several neuroimaging studies have identified specific brain regions most prominently affected by the disease [46]. The feature depicted in Figure 10 (b) highlights the relative significance of superior frontal gyrus region. Metabolic changes in this particular region has been associated with cognitive decline [47]. In addition to these overall features, we identified a feature that emphasized the potential contribution of a specific brain region for AD diagnosis. Figures 10 (c) and (d) display the same feature that illustrates the importance of vermis region of the cerebellum with intensity differences between the normal and AD subjects respectively. This particular region has been implicated to be affected in the early stages of the disease [48] which could be crucial for timely diagnosis.

It was very encouraging to detect internal features from the global module that exhibited strong connotations characteristic of Alzheimer's disease. Unfortunately, as the individual subnetworks of the local generator module are trained independently, the concatenated versions of the local features were not easy to decipher. Subsequently, we found it difficult to identify feature maps from the end-layer that could be interpreted in terms of contributions associated with global and local components.

2) Interpolation: GANs are prone to overfitting; more so with medical images that have high dimensionality and low sample size. To ensure that our model is not memorizing training images, we performed linear interpolation in MRI space between two MR images chosen from different classes to clearly see the effect of the transition from one class to the other. Then, PET scans corresponding to interpolated MR images are generated using our model. If the model is overfitting, we expect to see discrete transitions in the interpolated images [45] As Figure 11 shows, the generated PET scans follow a smooth transition with no artifacts indicating that the model has learned the underlying distribution well. Moreover, we classified the generated scans from interpolation, and as expected, the probability of being classified as normal also changes gradually from high to low as we approach AD.

E. Limitations

Our work also has some limitations which need to be acknowledged. Firstly, the introduction of local sub-networks to capture finer texture details leads to increase in the number of network parameters compared to the competing global methods. We believe that using more semantically segmented patches and exploiting sparsity constraints in the future can lead to the development of more optimized networks that provide similar performance.

Secondly, the focus of this study has been limited to discriminating AD from cognitively normal (CN). However, mild cognitive impairment (MCI) is considered as an intermediate state between normal aging and onset of AD. Further validation is needed to assess the effectiveness of the proposed GLA-GAN for a 3-way classification (AD-MCI-CN) which is very crucial for early diagnosis.

Lastly, an exhaustive search was not conducted to find all or the most meaningful internal GAN units. Due to the high dimensionality of the images being handled as well as the large number of internal units, identifying meaningful features is a very tedious and time-consuming task. Future efforts can be directed towards more systematic approaches that rely on agreement between activation units and anatomically segmented synthetic scans. Along the lines of [49], it would be very interesting to explore the causal effect of interpretable units in explaining Alzheimer's disease progression.

V. Conclusion

In this paper, we have presented a globally and locally aware GAN framework for MRI to PET cross-modality transfer. The proposed multi-path GAN architecture aids in concurrently capturing both global structure as well as local texture to

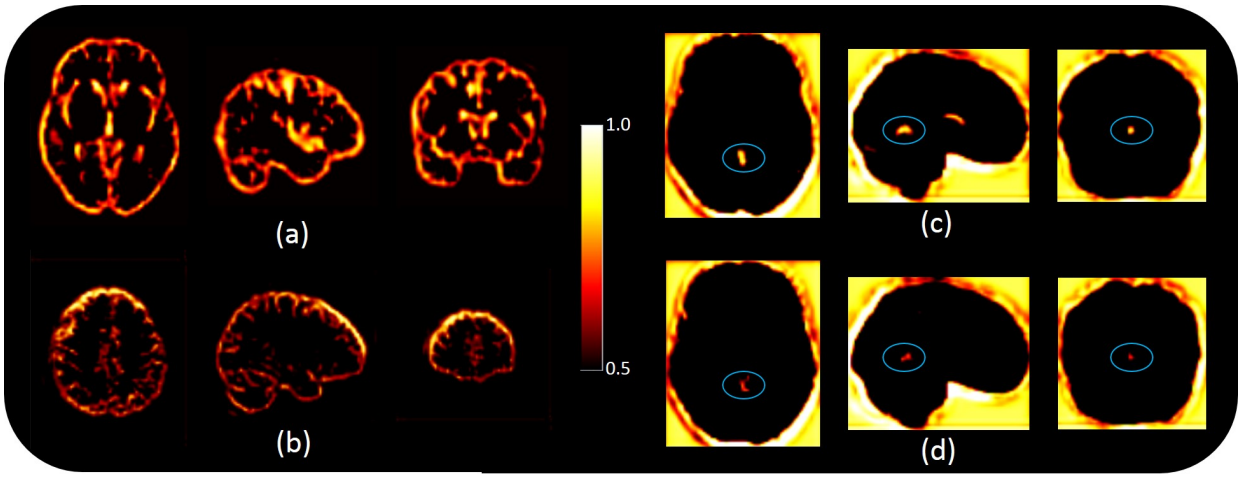


Fig. 10: Visualization of internal features from global module: (a) Feature that detects the overall uptake pattern covering regions most commonly associated with AD (cortex, subcortex, ventricles, etc.) (b) Feature that perceives relatively significant importance of superior frontal gyrus in AD (c) & (d) Feature that detects the vermis region of the cerebellum (associated with early stages of AD) validated by intensity differences between a CN and an AD sample respectively.

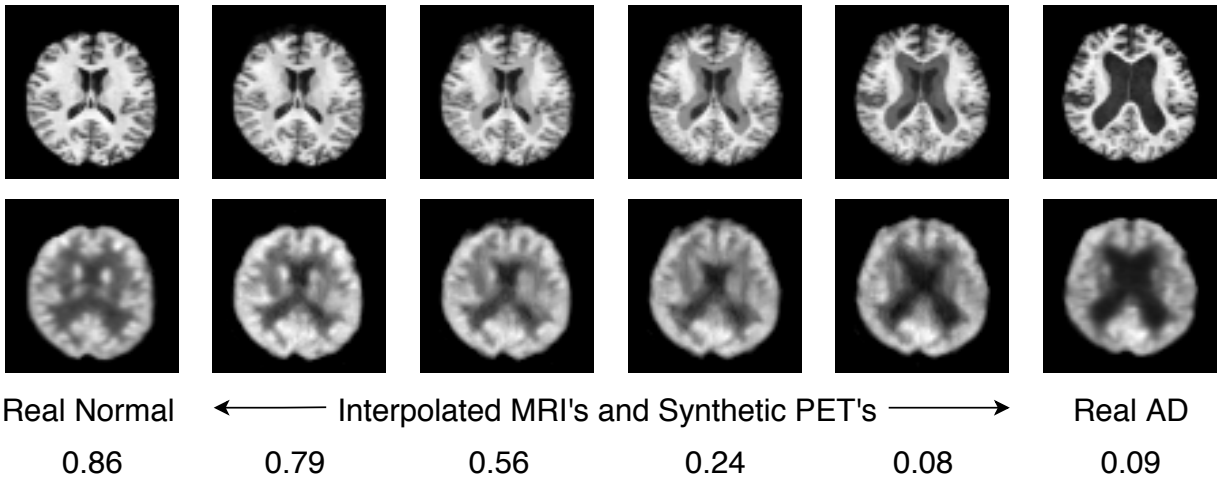


Fig. 11: MRI interpolations between one Normal and AD pair. Left-most and right-columns show pairs of real MRI and PET scans. Intermediate columns depict linear interpolations in the MRI space and their corresponding generated PET scans. Last row of numbers indicates the classification probability as Normal.

enhance the quality of synthesized PET scans. Furthermore, the standard adversarial loss in GANs is supplemented with L_1 loss to ensure voxel level fidelity of intensity values, MS-SSIM loss to ensure structural consistency at multiple scales and ROI loss to enforce local contextual integrity to discern variation in regional sensitivity to AD. The overall framework along with the combined synthesis objective function was designed to help the generative model to reliably learn the underlying bimodal data distribution. Experimental results demonstrate that our model not only generates PET scans with better image quality but also enriched features that improve AD diagnostic accuracy compared to state-of-the-art methods. Finally, our attempt to visualize intermediate feature maps exhibits the aptitude of GLA-GAN to automatically detect both common and differential FDG uptake patterns in PET images.

REFERENCES

[1] Marco Lorenzi, Ivor J Simpson, Alex F Mendelson, Sjoerd B Vos, M Jorge Cardoso, Marc Modat, Jonathan M Schott, and Sebastien Ourselin. Multimodal image analysis in alzheimer's disease via statistical modelling of non-local intensity correlations. *Scientific reports*, 6, 2016.

[2] K. R. Gray, R. Wolz, S. Keihaninejad, R. A. Heckemann, P. Aljabar, A. Hammers, and D. Rueckert. Regional analysis of fdg-pet for use in the classification of alzheimer's disease. In *2011 IEEE International Symposium on Biomedical Imaging: From Nano to Macro*, pages 1082–1085, 2011.

[3] Keith A Johnson, Nick C Fox, Reisa A Sperling, and William E Klunk. Brain imaging in alzheimer disease. *Cold Spring Harbor perspectives in medicine*, 2(4):a006213, 2012.

[4] Xin Y Zhang, Zhen L Yang, Guang M Lu, Gui F Yang, and Long J Zhang. Pet/mr imaging: new frontier in alzheimer's disease and other dementias. *Frontiers in molecular neuroscience*, 10:343, 2017.

[5] D. Cheng and M. Liu. Cnns based multi-modality classification for ad diagnosis. In *2017 10th International Congress on Image and*

Signal Processing, BioMedical Engineering and Informatics (CISP-BMEI), pages 1–5, 2017.

[6] Tri Huynh, Yaozong Gao, Jiayin Kang, Li Wang, Pei Zhang, Jun Lian, and Dinggang Shen. Estimating ct image from mri data using structured random forest and auto-context model. *IEEE transactions on medical imaging*, 35(1):174–183, 2015.

[7] Jiayin et al. Kang. Prediction of standard-dose brain pet image by using mri and low-dose brain [18f]fdg pet images. *Medical Physics*, 42(9):5301–5309, 2015.

[8] Amod Jog, Aaron Carass, Dzung L Pham, and Jerry L Prince. Random forest flair reconstruction from t 1, t 2, and p d-weighted mri. In *2014 IEEE 11th International Symposium on Biomedical Imaging (ISBI)*, pages 1079–1082. IEEE, 2014.

[9] Ian Goodfellow, Jean Pouget-Abadie, Mehdi Mirza, Bing Xu, David Warde-Farley, Sherjil Ozair, Aaron Courville, and Yoshua Bengio. Generative adversarial nets. In *Advances in neural information processing systems*, pages 2672–2680, 2014.

[10] Alec Radford, Luke Metz, and Soumith Chintala. Unsupervised representation learning with deep convolutional generative adversarial networks. *arXiv preprint arXiv:1511.06434*, 2015.

[11] Han Zhang, Tao Xu, Hongsheng Li, Shaoting Zhang, Xiaogang Wang, Xiaolei Huang, and Dimitris N Metaxas. Stackgan: Text to photo-realistic image synthesis with stacked generative adversarial networks. In *Proceedings of the IEEE international conference on computer vision*, pages 5907–5915, 2017.

[12] Qingsong Yang, Pingkun Yan, Yanbo Zhang, Hengyong Yu, Yongyi Shi, Xuanqin Mou, Mannudeep K Kalra, Yi Zhang, Ling Sun, and Ge Wang. Low-dose ct image denoising using a generative adversarial network with wasserstein distance and perceptual loss. *IEEE transactions on medical imaging*, 2018.

[13] Jelmer M Wolterink, Anna M Dinkla, Mark HF Savenije, Peter R Seevinck, Cornelis AT van den Berg, and Ivana Išgum. Deep mr to ct synthesis using unpaired data. In *International Workshop on Simulation and Synthesis in Medical Imaging*. Springer, 2017.

[14] Maayan Frid-Adar, Idit Diamant, Eyal Klang, Michal Amitai, Jacob Goldberger, and Hayit Greenspan. Gan-based synthetic medical image augmentation for increased cnn performance in liver lesion classification. *Neurocomputing*, 321:321–331, 2018.

[15] Changhee Han, Hideaki Hayashi, Leonardo Rundo, Ryosuke Araki, Wataru Shimoda, Shinichi Muramatsu, Yujiro Furukawa, Giancarlo Mauri, and Hideki Nakayama. Gan-based synthetic brain mr image generation. In *2018 IEEE 15th International Symposium on Biomedical Imaging (ISBI 2018)*, pages 734–738. IEEE, 2018.

[16] Zhongyi Han, Benzheng Wei, Ashley Mercado, Stephanie Leung, and Shuo Li. Spine-gan: Semantic segmentation of multiple spinal structures. *Medical image analysis*, 50:23–35, 2018.

[17] Vasileios Sevetlidis, Mario Valerio Giuffrida, and Sotirios A Tsaftaris. Whole image synthesis using a deep encoder-decoder network. In *International Workshop on Simulation and Synthesis in Medical Imaging*, pages 127–137. Springer, 2016.

[18] Diederik P Kingma and Max Welling. Auto-encoding variational bayes. *arXiv preprint arXiv:1312.6114*, 2013.

[19] Dong Nie, Roger Trullo, Jun Lian, Caroline Petitjean, Su Ruan, Qian Wang, and Dinggang Shen. *Medical image synthesis with context-aware generative adversarial networks*, volume 10435 of *Lecture Notes in Computer Science*, pages 417–425. Springer, 2017.

[20] Cheng-Bin Jin, Wonmo Jung, Seongsu Joo, E. Park, Young Saem Ahn, I. H. Han, J. Lee, and X. Cui. Deep ct to mr synthesis using paired and unpaired data. *Sensors*, 2019.

[21] Avi Ben-Cohen, Eyal Klang, Stephen P Raskin, Shelly Soffer, Simona Ben-Haim, Eli Konen, Michal Marianne Amitai, and Hayit Greenspan. Cross-modality synthesis from ct to pet using fcn and gan networks for improved automated lesion detection. *Engineering Applications of Artificial Intelligence*, 2019.

[22] Wen Wei, Emilie Poirion, Benedetta Bodini, Stanley Durrleman, Nicholas Ayache, Bruno Stankoff, and Olivier Colliot. Predicting pet-derived demyelination from multimodal mri using sketcher-refiner adversarial training for multiple sclerosis. *Medical image analysis*, 58:101546, 2019.

[23] Rongjian Li, Wenlu Zhang, Heung-Il Suk, Li Wang, Jiang Li, Dinggang Shen, and Shuiwang Ji. Deep learning based imaging data completion for improved brain disease diagnosis. In *MICCAI*, volume 8675 of *Lecture Notes in Computer Science*, pages 305–312. Springer, 2014.

[24] Apoorva Sikka, Skand Vishwanath Peri, and Deepti.R Bathula. Mri to fdg-pet: Cross-modal synthesis using 3d u-net for multi-modal alzheimer's classification. In *MICCAI Workshop on Simulation and Synthesis in Medical Imaging*, 2018.

[25] Yongsheng Pan, Mingxia Liu, Chunfeng Lian, Tao Zhou, Yong Xia, and Dinggang Shen. Synthesizing missing pet from mri with cycle-consistent generative adversarial networks for alzheimer's disease diagnosis. In *International Conference on Medical Image Computing and Computer-Assisted Intervention*, 2018.

[26] Haoliang Sun, Ronak Mehta, Hao H. Zhou, Zhichun Huang, Sterling C. Johnson, Vivek Prabhakaran, and Vikas Singh. Dual-glow: Conditional flow-based generative model for modality transfer. In *The IEEE International Conference on Computer Vision (ICCV)*, October 2019.

[27] Durk P Kingma and Prafulla Dhariwal. Glow: Generative flow with invertible 1x1 convolutions. In *Advances in neural information processing systems*, pages 10215–10224, 2018.

[28] Justin Johnson, Alexandre Alahi, and Li Fei-Fei. Perceptual losses for real-time style transfer and super-resolution. In *European conference on computer vision*, pages 694–711, 2016.

[29] Zhou Wang, Eero P Simoncelli, and Alan C Bovik. Multiscale structural similarity for image quality assessment. In *The Thrity-Seventh Asilomar Conference on Signals, Systems & Computers, 2003*. Ieee, 2003.

[30] K. He, X. Zhang, S. Ren, and J. Sun. Deep residual learning for image recognition. In *2016 IEEE Conference on Computer Vision and Pattern Recognition (CVPR)*, pages 770–778, 2016.

[31] S. Ioffe and Christian Szegedy. Batch normalization: Accelerating deep network training by reducing internal covariate shift. *ICML*, 2015.

[32] V. Nair and Geoffrey E. Hinton. Rectified linear units improve restricted boltzmann machines. In *ICML*, 2010.

[33] Alec Radford, Luke Metz, and Soumith Chintala. Unsupervised representation learning with deep convolutional generative adversarial networks. In *International Conference on Learning Representations*, 2016.

[34] Sergey Ioffe and Christian Szegedy. Batch normalization: Accelerating deep network training by reducing internal covariate shift. In *Proceedings of the 32nd International Conference on Machine Learning*, 2015.

[35] Zhou Wang, Eero P Simoncelli, and Alan C Bovik. Multiscale structural similarity for image quality assessment. In *The Thrity-Seventh Asilomar Conference on Signals, Systems & Computers, 2003*, volume 2, pages 1398–1402. Ieee, 2003.

[36] Brian A Gordon, Tyler Blazey, and Tammie LS Benzinger. Regional variability in alzheimer's disease biomarkers. *Future neurology*, 9(2):131–134, 2014.

[37] Susanne G Mueller, Michael W Weiner, Leon J Thal, Ronald C Petersen, Clifford Jack, William Jagust, John Q Trojanowski, Arthur W Toga, and Laurel Beckett. The alzheimer's disease neuroimaging initiative. *Neuroimaging Clinics of North America*, 15(4):869–877, 2005.

[38] Clifford R Jack Jr, David S Knopman, William J Jagust, Leslie M Shaw, Paul S Aisen, Michael W Weiner, Ronald C Petersen, and John Q Trojanowski. Hypothetical model of dynamic biomarkers of the alzheimer's pathological cascade. *The Lancet Neurology*, 9(1):119–128, 2010.

[39] Clifford R Jack Jr, Matt A Bernstein, Nick C Fox, Paul Thompson, Gene Alexander, Danielle Harvey, Bret Borowski, Paula J Britson, Jennifer L. Whitwell, Chadwick Ward, et al. The alzheimer's disease neuroimaging initiative (adni): Mri methods. *Journal of Magnetic Resonance Imaging: An Official Journal of the International Society for Magnetic Resonance in Medicine*, 27(4):685–691, 2008.

[40] Nathalie Tzourio-Mazoyer, Brigitte Landeau, Dimitri Papathanassiou, Fabrice Crivello, Olivier Etard, Nicolas Delcroix, Bernard Mazoyer, and Marc Joliot. Automated anatomical labeling of activations in spm using a macroscopic anatomical parcellation of the mni mri single-subject brain. *Neuroimage*, 15(1):273–289, 2002.

[41] Juan Eugenio Iglesias, Cheng-Yi Liu, Paul M Thompson, and Zhuowen Tu. Robust brain extraction across datasets and comparison with publicly available methods. *IEEE transactions on medical imaging*, 30(9):1617–1634, 2011.

[42] Mark Jenkinson, Christian F Beckmann, Timothy EJ Behrens, Mark W Woolrich, and Stephen M Smith. Fsl. *Neuroimage*, 2012.

[43] Adam Paszke, Sam Gross, Soumith Chintala, Gregory Chanan, Edward Yang, Zachary DeVito, Zeming Lin, Alban Desmaison, Luca Antiga, and Adam Lerer. Automatic differentiation in pytorch. 2017.

[44] Diederik Kingma and Jimmy Ba. Adam: A method for stochastic optimization. In *International Conference on Learning Representations*, 12 2014.

[45] Augustus Odena, Christopher Olah, and Jonathon Shlens. Conditional image synthesis with auxiliary classifier gans. In *Proceedings of the 34th International Conference on Machine Learning-Volume 70*. JMLR. org, 2017.

[46] Russell P Sawyer, Federico Rodriguez-Porcel, Matthew Hagen, Rhonna Shatz, and Alberto J Espay. Diagnosing the frontal variant of alzheimer's

disease: a clinician's yellow brick road. *Journal of clinical movement disorders*, 4(1):2, 2017.

[47] Maria del C Valdés Hernández, Stuart Reid, Shadia Mikhael, Cyril Pernet, and Alzheimer's Disease Neuroimaging Initiative. Do 2-year changes in superior frontal gyrus and global brain atrophy affect cognition? *Alzheimer's & Dementia: Diagnosis, Assessment & Disease Monitoring*, 10(1):706–716, 2018.

[48] Heidi IL Jacobs, David A Hopkins, Helen C Mayrhofer, Emiliano Bruner, Fred W van Leeuwen, Wijnand Raaijmakers, and Jeremy D Schmahmann. The cerebellum in alzheimer's disease: evaluating its role in cognitive decline. *Brain*, 141(1):37–47, 2018.

[49] David Bau, Jun-Yan Zhu, Hendrik Strobelt, Bolei Zhou, Joshua B Tenenbaum, William T Freeman, and Antonio Torralba. Gan dissection: Visualizing and understanding generative adversarial networks. *arXiv preprint arXiv:1811.10597*, 2018.